

Freqformer: Image-Demoiréing Transformer via Efficient Frequency Decomposition

Xiaoyang Liu^{1*}, Bolin Qiu^{1*}, Jiezhang Cao²,
 Zheng Chen¹, Yulun Zhang^{1†}, Xiaokang Yang¹
¹Shanghai Jiao Tong University, ²Harvard University

Abstract

Image demoiréing remains a challenging task due to the complex interplay between texture corruption and color distortions caused by moiré patterns. Existing methods, especially those relying on direct image-to-image restoration, often fail to disentangle these intertwined artifacts effectively. While wavelet-based frequency-aware approaches offer a promising direction, their potential remains underexplored. In this paper, we present Freqformer, a Transformer-based framework specifically designed for image demoiréing through targeted frequency separation. Our method performs an effective frequency decomposition that explicitly splits moiré patterns into high-frequency spatially-localized textures and low-frequency scale-robust color distortions, which are then handled by a dual-branch architecture tailored to their distinct characteristics. We further propose a learnable Frequency Composition Transform (FCT) module to adaptively fuse the frequency-specific outputs, enabling consistent and high-fidelity reconstruction. To better aggregate the spatial dependencies and the inter-channel complementary information, we introduce a Spatial-Aware Channel Attention (SA-CA) module that refines moiré-sensitive regions without incurring high computational cost. Extensive experiments on various demoiréing benchmarks demonstrate that Freqformer achieves state-of-the-art performance with a compact model size. The code is publicly available at <https://github.com/xyLiu339/Freqformer>.

1 Introduction

Capturing digital screens with a camera often introduces moiré patterns—irregular, colorful artifacts caused by aliasing between the screen’s subpixel layout and the camera’s color filter array (CFA) [1]. These patterns significantly degrade image quality and are difficult to remove due to their complexity and variability. Consequently, single-image demoiréing remains a challenging low-level vision task that continues to attract attention from both academia and industry.

Recent advances in deep learning have led to progress in image demoiréing, with CNN-based models achieving promising results [2, 3, 4, 5, 6, 7, 8, 9]. However, most existing approaches treat moiré removal as a holistic restoration task, directly learning to map the input image to a clean output. This straightforward strategy is inherently limited due to the complex nature of moiré patterns: the **color distortions** caused by moiré patterns are mixed with the original image colors, and the **corrupted textures** often resemble natural structures. To address this, some recent works have turned to wavelet-based frequency decomposition, *e.g.*, the Haar transform, to disentangle image components. While frequency-aware methods have shown improved performance, their potential has not been fully explored. For instance, some methods [10, 11] simply concatenate wavelet subbands for joint learning, failing to exploit the distinct semantics of different frequency components. Other methods [12] use complex multi-stage multi-branch architectures, which introduce design complexity and suffer from accumulated reconstruction errors.

*Equal contribution

†Corresponding author: Yulun Zhang, yulun100@gmail.com

To overcome these limitations, we introduce a novel frequency decomposition to efficiently **separate moiré textures and color distortions into high-frequency and low-frequency components**, respectively (Fig. 1). This enables the design of a dual-branch architecture that learns to handle each frequency band independently, providing more specialized restoration. In addition, benefiting from the favorable properties of our frequency decomposition, the high-frequency moiré textures exhibit strong **locality**, while the low-frequency components demonstrate **robustness to scale variations**. Leveraging these characteristics, we adopt crop-based training for high-frequency features and resize-based training for low-frequency features, leading to improved performance. Moreover, while traditional wavelet methods rely on predefined, non-trainable inverse transforms, our decomposition is designed to support a learnable **Frequency Composition Transform (FCT)** module, which adaptively fuses the two branches and ensures better consistency in reconstruction.



Figure 1: Frequency Decomposition.

Additionally, most previous demoiréing methods are built on heavy U-Net-style backbones [3, 4, 2, 7] (10M~50M), which, while effective, are computationally inefficient—especially for ultra-high-resolution images (e.g., 4K). Recent findings [9] have also shown that moiré artifacts exhibit variance across color channels, which motivates more refined attention mechanisms. To this end, we introduce a **Spatial-Aware Channel Attention (SA-CA)** module that enhances both spatial and channel-wise feature modeling while maintaining a compact design. Unlike standard attention modules, SA-CA selectively emphasizes moiré-prone regions and channels without incurring excessive computational overhead, making our model suitable for high-resolution inference and deployment on edge devices.

By integrating the above components, we propose **Freqformer**, a hierarchical dual-branch Transformer tailored for image demoiréing. Freqformer leverages frequency feature separation, adaptive fusion, and efficient attention mechanisms to remove moiré artifacts. It achieves state-of-the-art performance on various high-resolution image demoiréing benchmarks, while maintaining a compact model size. Our main contributions are summarized as follows:

- We introduce a novel frequency decomposition strategy in the image demoiréing task to effectively separate moiré patterns into high-frequency (texture) and low-frequency (color) components, enabling targeted learning for each.
- We design a dual-branch architecture that separately processes high- and low-frequency components using crop- and resize-based training strategies, enabling specialized feature extraction tailored to different aspects of moiré patterns. We also introduce a learnable FCT module that adaptively fuses the outputs from both branches.
- We propose our dual-branch hierarchical transformer, Freqformer, with a lightweight SA-CA module to enhance both spatial and channel-wise feature interactions. Extensive experiments on high-resolution image demoiréing benchmarks show that Freqformer achieves state-of-the-art performance with a relatively small number of parameters.

2 Related Works

2.1 Demoiréing Methods

Image demoiréing. Early image demoiréing methods focused on specific moiré patterns. These approaches, such as smooth filtering [13], spectral analysis [14], and image decomposition [15], rely heavily on handcrafted features and mathematical models and often fail to generalize effectively to diverse moiré patterns and varying image conditions. In recent years, deep learning-based methods [2, 3, 4, 5, 6, 16] have emerged as a powerful tool for image demoiréing. Yu et al. [7] proposed ESDNet, the first lightweight model for ultra-high-resolution image demoiréing. MoiréDet, put forward by Yang et al. [17], further extracts moiré edge maps from images with moiré patterns using a triplet generation strategy. Peng et al. [18] presents DMSFN, a network using dilated-dense attention and multiscale feature interaction for effective Moiré pattern removal, along with a moiré data augmentation technique. Xiao et al. [9] developed a patch bilateral compensation network (P-BiC) for ultra-high-definition image demoiréing, leveraging the green channel’s resistance to moiré patterns. FHDe2Net [2] removes moiré patterns using a global-to-local structure, and extracts the luminance channel from the original image in the YUV color space to compensate for high-frequency detail loss caused by downsampling. However, frequency decomposition is only used as a detail compensation module, and the YUV decomposition disrupts the original inter-channel correlations in the RGB space, leading to incomplete moiré removal.

Video demoiréing. Video demoiréing poses added challenges due to the need for temporal coherence. Dai et al. [19] introduced the first hand-held video demoiréing dataset and a baseline model using relation-based temporal consistency loss. Cheng et al. [20] extended image and video demoiréing to Raw inputs with color-separated and spatial modulations. Xu et al. [21] proposed DTNet, a unified framework that performs moiré removal, alignment, color correction, and detail refinement via directional DCT modes and a temporal-guided bilateral learning pipeline.

Raw domain demoiréing. The Raw domain offers high-bit-depth data with reduced ISP interference, making it well-suited for low-level tasks. This is especially true for demoiréing, where moiré patterns are simpler in Raw [22], free from ISP-induced nonlinearities. RDNet [22] first tackles Raw image demoiréing with an encoder-decoder and class-specific learning. RawVDemoiré [20] addresses video demoiréing via temporal alignment. Recent work [8] jointly leverages Raw and sRGB inputs to learn device-dependent ISP models for restoration. Raw-domain demoiréing may suffer from color shifts after ISP processing and the Raw data itself is also sensor-dependent. Therefore, in this work, we perform demoiréing directly in the RGB domain, aiming to model the mapping between RGB space and the real-world scene more effectively.

Moiré removal dataset. Sun et al. [5] introduced a large-scale benchmark dataset (TIP-2018) containing over 100,000 image pairs. Building upon the previous efforts, Zheng et al. [4] proposed the AIM2019 image demoiréing challenge dataset (LCDMoiré) in 2020, which consists of 10,200 synthetically generated image pairs. FHDMi dataset, presented by He et al. [2], provides high-resolution images with more diverse and complex moiré patterns. More recently, Yu et al. [7] took a further step by constructing the first large-scale real-world Ultr-High-Definition demoiréing dataset (UHDM), containing 5,000 real-world 4K resolution image pairs with more challenging and practical scenarios. Yue et al. [22] built the first well-aligned raw moiré image dataset (TMM-2022) by pixel-wise alignment between the recaptured images and source ones. LCDMoiré contains only text scenes and lacks diversity, while TIP-2018 does not include text scenes but has a limited resolution of only 256×256 . In contrast, FHDMi and UHDM offer a wide variety of scenes with sufficiently high resolution and greater complexity. Therefore, we adopt FHDMi and UHDM in our work.

2.2 Wavelet-based Methods

Wavelet-based methods, due to their ability to decompose an image into multiple frequency bands, have been widely applied in some computer vision tasks, including classification[23][24][25][26], network compression[27][28], face aging[29], super-resolution[30][31], style transfer[32], etc. In recent years, wavelet-based methods have emerged as powerful tools for image demoiréing. Liu et al. [11] proposed a wavelet-based dual-branch network (WDNet) that operates in the wavelet domain to effectively separate moiré patterns from image content by leveraging dense and dilated convolution modules. Luo et al. [10] propose AWUDN, a deep network that combines wavelet-domain feature mapping with a domain adaptation mechanism. Nevertheless, these two methods simply mix different frequency features without fully exploiting the hierarchical frequency features of wavelet decomposition. Further, Yeh et al. [12] introduced a multibranch wavelet-based network (MBWDN) that decomposes moiré images into multiple sub-band images using wavelet transform and processes them through different branches. However, due to its multi-level structure, the method incurs relatively high computational cost. Additionally, the use of the Haar transform leads to incomplete separation of moiré patterns, which limits its effectiveness when dealing with high-definition or complex cases.

3 Method

Our whole pipeline is shown in Fig. 3. Given a moiré image I_m , we first apply a frequency decomposition (Sec. 3.1) to obtain a high-frequency component I_h and a low-frequency component I_l , both retaining the original spatial resolution. During training, the high-frequency branch adopts a cropping strategy, while the low-frequency branch uses resizing (Sec. 3.2). In the testing phase, both branches operate on the full-resolution image. This decomposition enables the network to focus on frequency-specific characteristics, which are critical for effective moiré pattern removal.

The two branches process I_h / I_l using the encoder-decoder architecture. Each encoder and decoder block is a Spatial-Aware Channel Attention (SA-CA) module (Sec. 3.2) that contains a Residual Dilated Dense Block (RDDB) [33, 34, 35, 36] to effectively capture both local and contextual information and N transformer layers with channel attention and gated feed-forward networks, to dynamically integrate spatial and channel-wise features and enhance the representation capability.

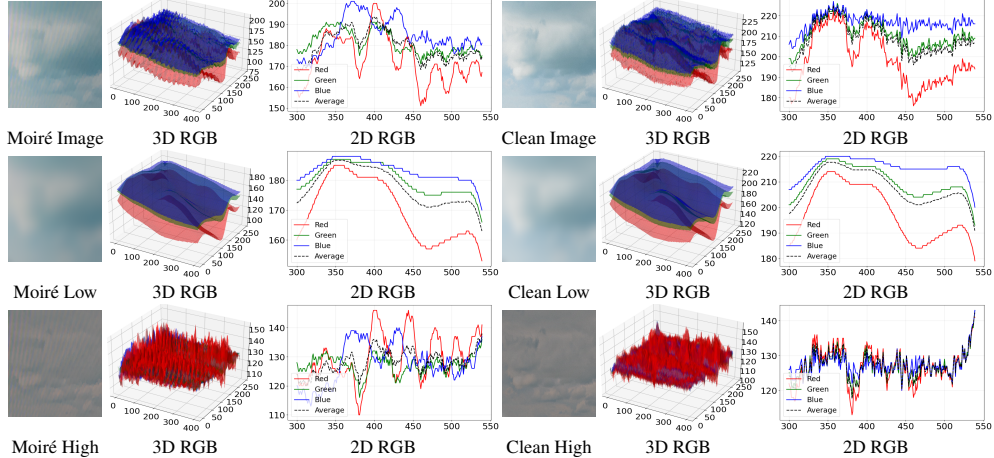


Figure 2: Visualization of the frequency-decomposed images (zoom in for better analysis). The left three columns show the moiré images along with their 2D and 3D visualizations, while the right three columns display the clean images. The first, second, and third rows represent the original images, low- and high-frequency components, respectively. The low-frequency curves of moiré and clean images exhibit similar trends, primarily reflecting color distortions. The high-frequency curves differ significantly in shape, indicating structural differences caused by moiré patterns.

To further support learning and refinement, the decoder at each level produces intermediate outputs, which provide deep supervision [4] signals that stabilize training and promote convergence. Moreover, a hierarchical feature fusion strategy (Sec. 3.2) is adopted in the high-frequency branch, where multi-scale features are concatenated with minimal overhead.

The network is trained in a two-phase manner (Sec. 3.3): initially, the high-frequency and low-frequency branches are trained independently to specialize in their respective frequency domains. After this, both branches are jointly fine-tuned along with a learnable Frequency Composition Transform (FCT) (Sec. 3.1), which fuses the final features from both branches and then reconstructs the clean output image with more accurate and visually pleasing results .

3.1 Frequency Decomposition and Learnable FCT

As shown in Fig. 2, we decompose both the moiré-contaminated image and the clean image into high- and low-frequency components and visualize the 2D/3D RGB curves. It is evident that the moiré patterns are predominantly preserved in the high-frequency part, while the low-frequency component exhibits minimal moiré textures but suffers from noticeable color distortions. Notably, although the low-frequency curve of the moiré image follows a similar overall trend to that of the clean image, there is a significant deviation in magnitude. This discrepancy can be attributed to two main factors. First, the presence of moiré patterns inherently distorts the original color information during the frequency decomposition, which complicates the accurate recovery of low-frequency components and remains a significant challenge. Second, the dataset construction process itself introduces severe color mismatches — or more precisely, color shifts (also mentioned in [1, 4, 9]) — due to varying external conditions such as lighting during the moiré image capture in the dataset construction process. Therefore, following the frequency decomposition, we design a dual-branch approach (will be detailed in Sec. 3.2): a high-frequency branch dedicated to restoring fine textures affected by moiré patterns, and a low-frequency branch focused on recovering accurate color information, addressing both moiré-induced distortions and dataset-related color shifts.

As demonstrated above, frequency decomposition plays a crucial role in our framework. However, conventional tools such as the multi-level Haar wavelet transform (used in [10, 11, 12]) are not well-suited to our design needs. The primary limitation is that, despite multiple levels of decomposition (*e.g.*, from $H \times W$ to $H/2^i \times W/2^i$ for level i), the moiré patterns often remain in the final low-frequency component. This indicates that the Haar transform is neither efficient nor effective in separating moiré textures. More critically, the final low-frequency output is typically discrete pixel values, so any restoration error in this stage will accumulate during reconstruction, ultimately leading to significant pixel-level inaccuracies in the recomposed image. To overcome these issues, we utilize a frequency transform that better separates moiré artifacts and supports a more training-friendly framework.

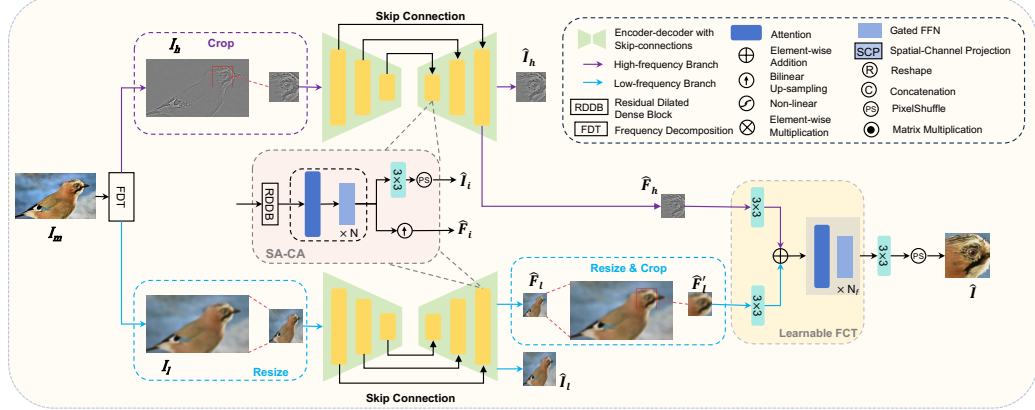


Figure 3: The whole pipeline of our Freqformer. The figure shows the dual-branch learning with crop/resize strategy and a learnable FCT module.

Inspired by [37], our decomposition design is as follows. Given a moiré image I_m , we utilize convolution with kernel k , which is defined as

$$k = \begin{bmatrix} 1/16 & 1/8 & 1/16 \\ 1/8 & 1/4 & 1/8 \\ 1/16 & 1/8 & 1/16 \end{bmatrix}. \quad (1)$$

The decomposition is comprised of L -level and is a recursive process. For level i 's decomposition process ($i = 1, 2, \dots, L$), the decomposition outcome I_l^i and I_h^i is calculated as

$$I_l^i = \text{Conv}(I_l^{i-1}, k, i), \quad I_h^i = I_h^{i-1} + I_l^{i-1} - I_l^i, \quad (2)$$

where $I_l^0 = I_m$, $I_h^0 = 0$ and Conv represents the convolution with a dilation of 2^i . Ultimately, the L -level decomposition results of image I are obtained as $I_l = I_l^L$ and $I_h = I_h^L$.

After the dual-branch demoiré process, we can get the clean representation \hat{I}_l and \hat{I}_h . Normally, according to Eq. 2, the final output is calculated as

$$\hat{I} = \hat{I}_l + \hat{I}_h, \quad (3)$$

But this traditional composition process can not fuse the two branch effectively, as the reconstruction error on the same area on the low and high frequency will further lead to more severe distortions. So we instead design a learnable Frequency Composition Transform (FCT) which operates on the feature space. According to Fig. 3, we extract the feature before the convolution that projects the feature dimension to image dimension and the PixelShuffle, and denote it as \hat{F}_l and \hat{F}_h . The learnable FCT module is defined as

$$F = \text{Conv}(\hat{F}_l) + \text{Conv}(\hat{F}_h), \quad \hat{F} = \text{PostFusion}(F), \quad (4)$$

$$\hat{I} = \text{PixelShuffle}(\text{Conv}(\hat{F})). \quad (5)$$

The addition of the separate convolution outputs is mathematically equivalent to $F = \text{Conv}(\text{Concat}(\hat{F}_l, \hat{F}_h))$, but doubles the number of bias parameters. The *PostFusion* module is an N_f layer's transformer block, which will be detailed in Sec. 3.2.

3.2 Dual-Branch Design and the SA-CA Module

After decomposing the clean image I_m into I_l and I_h , there shows some awesome benefits:

1. The high-frequency component shows strong spatial locality, carrying little color and mainly encoding texture. Thus, only local context is needed for effective demoiré, making the global image structure less important. This allows robust training via random cropping and direct application to ultra-high-resolution demoiré tasks.
2. The low-frequency component is smooth and highly scale-robust. It can be downsampled to a much lower resolution (e.g., 0.1×) and still be accurately reconstructed. We experimented with I_h and I_l separately resized and then restored to their original size to assess information loss. Results show reconstruction PSNRs of ~ 30 dB (I_h) and ~ 50 dB (I_l), confirming that I_l can be safely resized with minimal degradation.

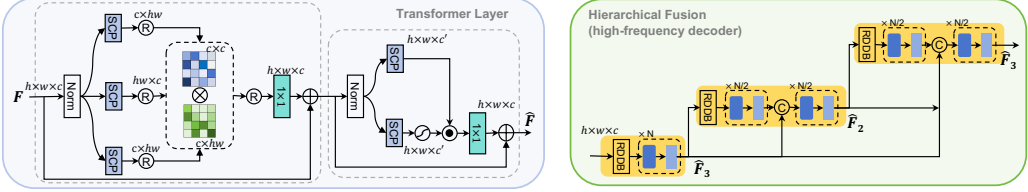


Figure 4: Left part is the detailed transformer architecture of the SA-CA module utilized in all the encoders and decoders. The right part shows the hierarchical fusion of the high-frequency branch.

3. After resizing, moiré-induced color distortions become spatially concentrated. Consequently, only small, textureless patches with color deviations require correction, which still depends on local spatial features and channel-wise representations. Hence, using similar network structures for the high- and low-frequency branches is a natural and simplified choice.
4. Aggressively downsampling the low-frequency component simplifies color shift correction, as full color information is preserved compactly. This lets the low-frequency branch use the same small-scale input during both training and inference, avoiding issues with varying input sizes.

As analyzed above, we adopt a two-branch learning framework and apply cropping and resizing strategies to the high- and low-frequency branches, respectively, as shown in Fig. 3.

Spatial-Aware Channel Attention Module. Inspired by the work [9], which reveals that the green channel is less effected by the moiré patterns, and observing the visualization curves in Fig. 2, we find that the RGB curves are not the same and sometimes they show complementary effect, so we decide to let each channel fully attend to others and adjust the feature. We adopt the channel attention mechanism here, which is also commonly used in many tasks like [8, 38, 39]. However, only the channel information is insufficient to precisely restore a moiré image, spatial information is still important to learn from adjacent domain for both texture learning and color projection, as the frequency characteristics or directional patterns of a wave can only be inferred from multiple spatially adjacent points; a single point, in isolation, contains no frequency information. So we add the effective Residual Dilated Dense Block (RDDB) [33, 34, 35, 36] for information extraction with a larger receptive field. Apart from that, the projection layer in the attention and the FFN module is also important, which is expected to both aggregate the spatial feature and project the channel feature for local-feature and inter-channel learning.

Each block of the encoders and decoders uses the Spatial-Aware Channel Attention (SA-CA) Module. As shown in Fig. 4, our whole Spatial-Aware Channel Attention Module is defined as follows: Given an input feature $F \in \mathcal{R}^{h \times w \times c}$, it first goes through an RDDB block to extract the spatial information with a large receptive field. Then, it goes through N layers of transformer block, each consisting of a channel attention and a gated Feed-Forward Network. For the channel Attention, given the input F , we first generate the $Q, K, V \in \mathcal{R}^{h \times w \times c}$ using the spatial-channel projection. Considering efficiency and functionality, we finally utilize the 1×1 convolution followed by 3×3 depth-wise convolution, expecting the former to learn the channel pattern projection and the latter to aggregate the adjacent information. Then using reshape and transpose, we get $Q' \in \mathcal{R}^{c \times h \times w}$, $K' \in \mathcal{R}^{h \times w \times c}$ and $V' \in \mathcal{R}^{c \times h \times w}$. And then, we perform channel attention $\hat{F} = \text{Attention}(Q', K', V') + F$, with channels divided into heads to learn different features. As for the subsequent Feed-Forward Network, the traditional one can only conduct channel-wise learning and hardly handle the spatial-channel variant demoiréing task. As a result, we decide to let the FFN be a gated module that filters the inappropriate information. Firstly, through the spatial-channel projection (also a 1×1 convolution and a 3×3 depth-wise convolution), we get $X, Y \in \mathcal{R}^{h \times w \times c'}$. We utilize a non-linear function to get the filter scores and conduct the element-wise multiplication, followed by a convolution and a residual connection from the input F .

Apart from the block design, we also design the high-frequency decoder's hierarchical fusion. As sometimes the moiré texture may have a wide range of variety, the demoiré feature from the lower level of the decoder might help to produce the higher clean feature. We denote the output of each decoder block as $\hat{F}_3, \hat{F}_2, \hat{F}_1$. For the mid-block of the decoder, the \hat{F}_3 from the bottom block is concatenated into the medium output of the $N/2$ layers and then fed to the later $N/2$ layers for fusion. For the top block of the decoder, the \hat{F}_3 and \hat{F}_2 are concatenated into the middle output of the $N/2$ layers and then fed to the later $N/2$ layers for fusion.

3.3 Training Strategy and Loss Functions

The training is set in two stages. For stage one, the high-frequency branch and the low-frequency branch are trained separately, with the crop strategy and the resize strategy, respectively. And for stage two, we jointly trained the two branches and the learnable FCT. It is noteworthy that, due to the different crop / resize strategy, we first interpolate the $\hat{\mathbf{F}}_l$ to the original full size. Then based on the crop location (x_1, y_1, x_2, y_2) of $\hat{\mathbf{I}}_h$, we crop the interpolated feature $\hat{\mathbf{F}}'_l$ and feed both $\hat{\mathbf{F}}'_l$ and $\hat{\mathbf{F}}_h$ into the learnable FCT to get the final $\hat{\mathbf{I}}$.

For the loss function of the first stage, we take the deep supervision strategy proposed in [4]. The high- and low-branch loss function is defined as:

$$L_{stage_1}^{high} = \sum_{i=1}^3 (L_1(\hat{\mathbf{I}}_{h_i}, \mathbf{I}_{h_i}^{GT}) + \lambda_1 \times L_p(\hat{\mathbf{I}}_{h_i}, \mathbf{I}_{h_i}^{GT})). \quad (6)$$

$$L_{stage_1}^{low} = \sum_{i=1}^3 (L_1(\hat{\mathbf{I}}_{l_i}, \mathbf{I}_{l_i}^{GT}) + \lambda_1 \times L_p(\hat{\mathbf{I}}_{l_i}, \mathbf{I}_{l_i}^{GT})). \quad (7)$$

For the second stage, the loss function is defined as:

$$L_{stage_2} = L_1(\hat{\mathbf{I}}, \mathbf{I}^{GT}) + \lambda_2 \times L_p(\hat{\mathbf{I}}, \mathbf{I}^{GT}). \quad (8)$$

We use the perceptual loss from the pretrained VGG16 [40] Network. λ_1 and λ_2 are utilized to balance the two losses.

4 Experiments

Datasets and metrics. In the experiments, we separately train and test our Freqformer on the high-definition image dataset FHDMI [2], consisting of 9,981 and 2,019 pairs of images for training and testing with resolution 1920×1080 , and the ultra-high-definition (4K) image dataset UHDM [7], comprised of 4,500 and 500 pairs of images, while the testing is performed with a resolution of 3840×2160 , following [7]. To measure the performance of all models, we use PSNR, SSIM [41] and LPIPS [42] as the metrics. In general, higher PSNR and SSIM, as well as lower LPIPS, indicate higher quality of restored images. PSNR is more sensitive to color variations, SSIM better captures structural moiré patterns, and LPIPS aligns more closely with overall human perceptual quality [2].

Implementation details. We implement our algorithm using Pytorch on an NVIDIA RTX 4090 GPU. For training on the dataset FHDMI, we set the crop size as 512 and the resize size as 512. For UHDM, we set the crop and resize sizes as 768 and 512, respectively. We adopt the Adam optimizer [43] and the cyclic cosine schedule [44], with the initial learning rate of 0.0002, 150 epochs for both the training stages, and the batch size of 2. We set the $\lambda_1 = 1$ and $\lambda_2 = 0.1$ for simplicity. For the high-branch of the Freqformer, from the highest to the lowest resolution, the encoder's N is set to [2,2,2] and the decoder's N is set to [4,4,2]. For low-branch, both the encoder and decoder's N is [1,2,2]. N_f of the learnable FCT is set to 2.

4.1 Comparisons with State-of-the-Art Methods

Quantitative comparison. In Table 1, our proposed Freqformer achieves state-of-the-art performance compared with other methods, including DMCNN [5], MDDM [45], WDNNet [11], MopNet [3], MBCNN [4], FHDe²Net [2], and ESDNet [7]. On the FHDMI dataset, it significantly outperforms other methods by a large margin in all three evaluation metrics. This indicates superior reconstruction quality, structural fidelity, and perceptual similarity. On the more challenging UHDM dataset, our Freqformer ranks first in SSIM and LPIPS, and second in PSNR, closely following ESDNet-L. Notably, Freqformer achieves these competitive results with only 6.065M parameters, outperforming or matching methods with significantly larger model sizes (e.g., MopNet with 58.565M and MBCNN with 14.192M), highlighting its excellent trade-off between performance and model efficiency.

Additionally, in Table 2, we train and test the best up-to-date image restoration models [46, 47, 48] for comparison. The AdaIR* and MoCE-IR* denote direct testing with their all-in-one checkpoint, while without * represents the retraining on the two datasets. Our model surpasses all five models with a compact model size, only inferior to OSEDiff in LPIPS, which has nearly 1B parameters.

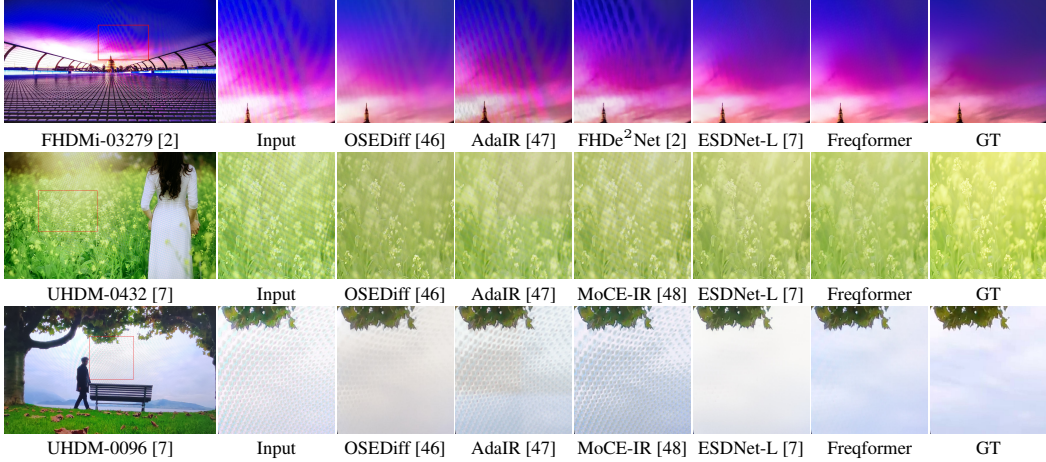


Figure 5: Visual comparisons of different baselines on FHDMi and UHDM datasets (please zoom in for better details). While OSEDiff, AdaIR, MoCE-IR, and FHDe²Net all struggle with removing moiré artifacts, ESDNet-L also leaves residual traces behind. In addition, these baselines suffer from color distortions and fail to accurately recover the original tones. In contrast, our approach effectively eliminates both moiré and color artifacts, as shown in the last row.

Table 1: Quantitative comparisons with demoiréing methods. **Red**: best and **Blue**: second-best

Dataset	Metrics	Input	DMCNN [5]	MDDM [45]	WDNet [11]	MopNet [3]	MBCNN [4]	FHDe ² Net [2]	ESDNet [7]	ESDNet-L [7]	Freqformer
FHDMi [2]	PSNR \uparrow	17.97	21.54	20.83	N/A	22.76	22.31	22.93	24.50	24.88	25.26
	SSIM \uparrow	0.7033	0.7727	0.7343	N/A	0.7958	0.8095	0.7885	0.8351	0.8440	0.8518
	LPIPS \downarrow	0.2837	0.2477	0.2515	N/A	0.1794	0.1980	0.1688	0.1354	0.1301	0.1253
UHDM [7]	PSNR \uparrow	17.12	19.91	20.09	20.36	19.49	21.41	20.34	22.12	22.42	22.22
	SSIM \uparrow	0.5089	0.7575	0.7441	0.6497	0.7572	0.7932	0.7496	0.7956	0.7985	0.8018
	LPIPS \downarrow	0.5314	0.3764	0.3409	0.4882	0.3857	0.3318	0.3519	0.2551	0.2454	0.2434
-	Params (M)	-	1.426	7.637	3.360	58.565	14.192	13.571	5.934	10.623	6.065

Table 2: Quantitative comparison with image restoration models. **Red**: best and **Blue**: second-best

Dataset	Metrics	OSEDiff [46]	AdaIR* [47]	AdaIR [47]	MoCE-IR* [48]	MoCE-IR [48]	Freqformer
FHDMi [2]	PSNR \uparrow	21.81	17.08	21.87	17.40	21.80	25.26
	SSIM \uparrow	0.7764	0.6986	0.8041	0.7031	0.7943	0.8518
	LPIPS \downarrow	0.1516	0.3057	0.1924	0.2969	0.2026	0.1253
UHDM [7]	PSNR \uparrow	20.66	16.68	20.96	16.97	20.46	22.22
	SSIM \uparrow	0.7607	0.4949	0.7807	0.4971	0.7644	0.8018
	LPIPS \downarrow	0.2394	0.5440	0.3040	0.5366	0.3249	0.2434
-	Params (M)	950	28.785	28.785	11.478	11.478	6.065

Qualitative comparison. Figure 5 presents visual comparisons of image restoration results on the FHDMi and UHDM datasets. Compared with existing methods, our Freqformer not only removes moiré more effectively, preserves fine details with high fidelity, but also mitigates the effects of color distortions and recovers the true color representation, resulting in more realistic and visually pleasing outputs. Competing methods such as OSEDiff, AdaIR, MoCE-IR, and FHDe²Net all struggle with moiré patterns that are embedded within the original content. Although ESDNet-L performs better than the other baselines, it still leaves behind residual moiré artifacts, as observed in the top two rows of Fig. 5. Moreover, as illustrated in the last row, ESDNet-L and all other baselines exhibit moiré-induced color distortions and fail to restore the original colors accurately. In contrast, our method successfully eliminates both the moiré patterns and color distortions. These results demonstrate Freqformer’s superior ability in both artifact removal and detail restoration, consistent with its leading quantitative performance in PSNR, SSIM, and LPIPS.

Model Complexity. As compared in Tabs. 1 and 2, our proposed Freqformer not only has fewer parameters compared to state-of-the-art image restoration methods such as AdaIR, MoCE-IR, and OSEDiff, but also achieves a smaller size than ESDNet-L, while delivering superior performance comparable to the small variant of ESDNet. Moreover, Freqformer requires only 2.49 TFLOPS to process 4K images in the UHDM dataset, which is on par with ESDNet (2.24T) and significantly lower than that of its large variant (3.68T), as well as AdaIR (31.06T) and MoCE-IR (5.43T).

4.2 Ablation Study

In this section, we conduct many ablation studies on FHDMI to demonstrate the efficacy of our network’s structure, the proposed frequency decomposition method, and the training strategy.

Low-frequency branch training via resize. As we proposed in our method, the resize operation contains many benefits during the low-branch training, which are demonstrated in Tab. 3. We also train an ESDNet-L (10M) to verify our findings in the same setting. We can find that cropping prevents the model from leveraging the low-frequency component’s inherent robustness to resizing and hinders effective global information aggregation for color correction, resulting in significant degraded performance. We even introduce a crop-tile-strategy (crop to 512×512 patches with 32 overlap for inference) for crop-training, but still inferior to the resize-strategy.

Learnable Frequency Composition Transform and dual-branch training. In Tab. 4, we demonstrate the importance of our frequency decomposition and two-branch training strategy. As shown, ESDNet and Freqformer, using end-to-end (e2e) learning without frequency decomposition, perform worse than the two-branch approach. Moreover, incorporating a learnable FCT improves fusion consistency and pattern coherence with few parameters.

Freqformer performance on each branch. Here we show the separate branch’s performance on the high- and low-frequency images. We train the ESDNet (6M) for the same setting as ours. According to Tab. 5, with half of the parameters, our low-branch surpasses the ESDNet and high-branch reaches comparable performance on PSNR and SSIM, while being superior on LPIPS.

Freqformer component ablation. As shown in Tab. 6, hierarchical fusion (denoted as H.F. in the Table) improves performance with minimal computational and parameter overhead. Replacing RDDB with deeper transformer layers for a fair model size comparison shows that RDDB is more efficient and outperforms the pure transformer design. Plus, more transformer layers will slow down the speed. As a result, we utilize the RDDB together with the H.F. in the high-branch decoder. The low-branch learning is relatively easier, so we remove the hierarchical fusion.

Our frequency decomposition vs. Haar wavelet-transform. We switch our frequency decomposition to the 2-level Haar transform that is used in [10] and train a new model. Although the loss normally decreases as our model, the test result is terrible, with PSNR 13.32, SSIM 0.2113, and LPIPS 0.7574. The demoiréed images by Haar transform suffer from severe color shift, and texture distortions caused by the Haar inverse transform.

5 Conclusion

In this paper, we propose Freqformer, a novel demoiréing framework that leverages frequency separation to address the complex moiré patterns. By introducing a tailored frequency decomposition strategy and a learnable FCT module, we effectively disentangle moiré artifacts into high-frequency textures and low-frequency color distortions, and design a dual-branch architecture and specialized learning strategies—crop-based training for high-frequency textures and resize-based training for low-frequency distortions. Additionally, we introduce a lightweight yet effective SA-CA module to boost moiré-sensitive feature learning while maintaining efficiency, making our model suitable for deployment on high-resolution images and edge devices. This study highlights how the integration of frequency decomposition, learnable fusion, and spatial-channel attention design contributes to the progress of image demoiréing, which remains an ongoing direction for future exploration.

Table 3: Low-branch resizing.

Model (Low branch)	PSNR	SSIM	LPIPS	Params (M)
Freqformer w/ crop	23.13	0.9220	0.0695	2.695
Freqformer w/ crop & tile	25.90	0.9363	0.0486	2.695
Freqformer w/ resize	29.90	0.9568	0.0291	2.695
ESDNet-L w/ crop	23.01	0.9192	0.0736	10.623
ESDNet-L w/ crop & tile	25.35	0.9295	0.0575	10.623
ESDNet-L w/ resize	30.39	0.9570	0.0277	10.623

resulting in significant degraded performance. We even introduce a crop-tile-strategy (crop to 512×512 patches with 32 overlap for inference) for crop-training, but still inferior to the resize-strategy.

Table 4: Effects of learnable FCT and frequency decomposition.

Model	PSNR	SSIM	LPIPS	Params (M)
ESDNet w/ learnable FCT	25.20	0.8511	0.1244	12.567
ESDNet w/ fixed FCT	25.11	0.8469	0.1296	11.868
ESDNet-L (e2e)	24.88	0.8440	0.1301	10.623
Freqformer w/ learnable FCT	25.26	0.8518	0.1253	6.065
Freqformer w/ fixed FCT	25.13	0.8478	0.1298	5.876
Freqformer-L (e2e)	23.92	0.8409	0.1284	5.851

Table 5: Comparison with ESDNet (6M).

Frequency Model	PSNR	SSIM	LPIPS	Params (M)
High	ESDNet	29.24	0.8807	0.1510
	Freqformer	29.20	0.8805	0.1468
Low	ESDNet	29.88	0.9541	0.0294
	Freqformer	29.90	0.9568	0.0291

Table 6: The ablation of the hierarchical fusion (H.F.) and the RDDB.

Model (High branch)	PSNR	SSIM	Params (M)	Speed (s)
Freqformer	29.02	0.8786	3.181	0.0054
Freqformer w/o H.F.	28.99	0.8782	2.997	0.0053
Freqformer w/o RDDB	29.01	0.8782	2.944	0.0058

References

- [1] Ce Wang, Bin He, Shengsen Wu, Renjie Wan, Boxin Shi, and Ling-Yu Duan. Coarse-to-fine disentangling demoiréing framework for recaptured screen images. *TPAMI*, 2023.
- [2] Bin He, Ce Wang, Boxin Shi, and Ling-Yu Duan. Fhde 2 net: Full high definition demoiréing network. In *ECCV*, 2020.
- [3] Bin He, Ce Wang, Boxin Shi, and Ling-Yu Duan. Mop moire patterns using mopnet. In *ICCV*, 2019.
- [4] Bolun Zheng, Shanxin Yuan, Gregory Slabaugh, and Ales Leonardis. Image demoiréing with learnable bandpass filters. In *ICCV*, 2020.
- [5] Yujing Sun, Yizhou Yu, and Wenping Wang. Moiré photo restoration using multiresolution convolutional neural networks. *TIP*, 2018.
- [6] Shanxin Yuan, Radu Timofte, Gregory Slabaugh, Aleš Leonardis, Bolun Zheng, Xin Ye, Xiang Tian, Yaowu Chen, Xi Cheng, Zhenyong Fu, et al. Aim 2019 challenge on image demoiréing: Methods and results. In *ICCVW*, 2019.
- [7] Xin Yu, Peng Dai, Wenbo Li, Lan Ma, Jiajun Shen, Jia Li, and Xiaojuan Qi. Towards efficient and scale-robust ultra-high-definition image demoiréing. In *ECCV*, 2022.
- [8] Shuning Xu, Binbin Song, Xiangyu Chen, Xina Liu, and Jiantao Zhou. Image demoiréing in raw and srgb domains. In *ECCV*, 2024.
- [9] Zeyu Xiao, Zhihe Lu, and Xinchao Wang. P-bic: Ultra-high-definition image moiré patterns removal via patch bilateral compensation. In *ACM MM*, 2024.
- [10] Xiaotong Luo, Jiangtao Zhang, Ming Hong, Yanyun Qu, Yuan Xie, and Cuihua Li. Deep wavelet network with domain adaptation for single image demoiréing. In *CVPRW*, 2020.
- [11] Lin Liu, Jianzhuang Liu, Shanxin Yuan, Gregory Slabaugh, Aleš Leonardis, Wengang Zhou, and Qi Tian. Wavelet-based dual-branch network for image demoiréing. In *ECCV*, 2020.
- [12] Chia-Hung Yeh, Chen Lo, and Cheng-Han He. Multibranch wavelet-based network for image demoiréing. *Sensors*, 2024.
- [13] Hasib Siddiqui, Mireille Boutin, and Charles A Bouman. Hardware-friendly descreening. *TIP*, 2009.
- [14] Denis N Sidorov and Anil Christopher Kokaram. Suppression of moiré patterns via spectral analysis. In *VCIP*, 2002.
- [15] Fanglei Liu, Jingyu Yang, and Huanjing Yue. Moiré pattern removal from texture images via low-rank and sparse matrix decomposition. In *VCIP*, 2015.
- [16] Yuxin Zhang, Mingbao Lin, Xunchao Li, Han Liu, Guozhi Wang, Fei Chao, Shuai Ren, Yafei Wen, Xiaoxin Chen, and Rongrong Ji. Real-time image demoiréing on mobile devices. *ICLR*, 2023.
- [17] Cong Yang, Zhenyu Yang, Yan Ke, Tao Chen, Marcin Grzegorzek, and John See. Doing more with moiré pattern detection in digital photos. *TIP*, 2023.
- [18] Yan-Tsung Peng, Chih-Hsiang Hou, You-Cheng Lee, Aiden J Yoon, Zihao Chen, Yi-Ting Lin, and Wei-Cheng Lien. Image demoiréing via multi-scale fusion networks with moiré data augmentation. *IEEE Sens. J.*, 2024.
- [19] Peng Dai, Xin Yu, Lan Ma, Baoheng Zhang, Jia Li, Wenbo Li, Jiajun Shen, and Xiaojuan Qi. Video demoiréing with relation-based temporal consistency. In *CVPR*, 2022.
- [20] Yijia Cheng, Xin Liu, and Jingyu Yang. Recaptured raw screen image and video demoiréing via channel and spatial modulations. *NeurIPS*, 2023.
- [21] Shuning Xu, Binbin Song, Xiangyu Chen, and Jiantao Zhou. Direction-aware video demoiréing with temporal-guided bilateral learning. In *AAAI*, 2024.
- [22] Huanjing Yue, Yijia Cheng, Yan Mao, Cong Cao, and Jingyu Yang. Recaptured screen image demoiréing in raw domain. *TMM*, 25, 2022.
- [23] Shin Fujieda, Kohei Takayama, and Toshiya Hachisuka. Wavelet convolutional neural networks for texture classification. *arXiv preprint arXiv:1707.07394*, 2017.

[24] Qiufu Li, Linlin Shen, Sheng Guo, and Zhihui Lai. Wavelet integrated cnns for noise-robust image classification. In *CVPR*, 2020.

[25] Edouard Oyallon, Eugene Belilovsky, and Sergey Zagoruyko. Scaling the scattering transform: Deep hybrid networks. In *ICCV*, 2017.

[26] Travis Williams and Robert Li. Wavelet pooling for convolutional neural networks. In *ICLR*, 2018.

[27] Lionel Gueguen, Alex Sergeev, Ben Kadlec, Rosanne Liu, and Jason Yosinski. Faster neural networks straight from jpeg. *NeurIPS*, 2018.

[28] A Levinskis. Convolutional neural network feature reduction using wavelet transform. *ELEKTRON ELEKTROTECH*, 2013.

[29] Yunfan Liu, Qi Li, and Zhenan Sun. Attribute-aware face aging with wavelet-based generative adversarial networks. In *CVPR*, 2019.

[30] Huaibo Huang, Ran He, Zhenan Sun, and Tieniu Tan. Wavelet-srnet: A wavelet-based cnn for multi-scale face super resolution. In *ICCV*, 2017.

[31] Pengju Liu, Hongzhi Zhang, Kai Zhang, Liang Lin, and Wangmeng Zuo. Multi-level wavelet-cnn for image restoration. In *CVPRW*, 2018.

[32] Jaejun Yoo, Youngjung Uh, Sanghyuk Chun, Byeongkyu Kang, and Jung-Woo Ha. Photorealistic style transfer via wavelet transforms. In *ICCV*, 2019.

[33] Yulun Zhang, Yapeng Tian, Yu Kong, Bineng Zhong, and Yun Fu. Residual dense network for image super-resolution. In *CVPR*, 2018.

[34] Gao Huang, Zhuang Liu, Kilian Q Weinberger, and Laurens van der Maaten. Densely connected convolutional networks. In *CVPR*, 2017.

[35] Kaiming He, Xiangyu Zhang, Shaoqing Ren, and Jian Sun. Deep residual learning for image recognition. In *CVPR*, 2016.

[36] Fisher Yu and Vladlen Koltun. Multi-scale context aggregation by dilated convolutions. *ICLR*, 2015.

[37] Jianyi Wang, Zongsheng Yue, Shangchen Zhou, Kelvin C.K. Chan, and Chen Change Loy. Exploiting diffusion prior for real-world image super-resolution. *IJCV*, 2024.

[38] Syed Waqas Zamir, Aditya Arora, Salman Khan, Munawar Hayat, Fahad Shahbaz Khan, and Ming-Hsuan Yang. Restormer: Efficient transformer for high-resolution image restoration. In *CVPR*, 2022.

[39] Zheng Chen, Yulun Zhang, Jinjin Gu, Linghe Kong, Xiaokang Yang, and Fisher Yu. Dual aggregation transformer for image super-resolution. In *ICCV*, 2023.

[40] Karen Simonyan and Andrew Zisserman. Very deep convolutional networks for large-scale image recognition. *ICLR*, 2015.

[41] Zhou Wang, Alan C Bovik, Hamid R Sheikh, and Eero P Simoncelli. Image quality assessment: from error visibility to structural similarity. *TIP*, 2004.

[42] Richard Zhang, Phillip Isola, Alexei A Efros, Eli Shechtman, and Oliver Wang. The unreasonable effectiveness of deep features as a perceptual metric. In *CVPR*, 2018.

[43] Diederik Kingma and Jimmy Ba. Adam: A method for stochastic optimization. In *ICLR*, 2015.

[44] Ilya Loshchilov and Frank Hutter. Sgdr: Stochastic gradient descent with warm restarts. In *ICLR*, 2017.

[45] Xi Cheng, Zhenyong Fu, and Jian Yang. Multi-scale dynamic feature encoding network for image demoiréing. In *ICCVW*, 2019.

[46] Rongyuan Wu, Lingchen Sun, Zhiyuan Ma, and Lei Zhang. One-step effective diffusion network for real-world image super-resolution. *NeurIPS*, 2024.

[47] Yuning Cui, Syed Waqas Zamir, Salman Khan, Alois Knoll, Mubarak Shah, and Fahad Shahbaz Khan. Adair: Adaptive all-in-one image restoration via frequency mining and modulation. In *ICLR*, 2025.

[48] Eduard Zamfir, Zongwei Wu, Nancy Mehta, Yuedong Tan, Danda Pani Paudel, Yulun Zhang, and Radu Timofte. Complexity experts are task-discriminative learners for any image restoration. In *CVPR*, 2025.